Editors' Suggestion | Featured in Physics

Visualization of Defect-Induced Interband Proximity Effect at the Nanoscale

Thomas Gozlinski,[1,*] Qili Li,[1,*,†] Rolf Heid,[2] Oleg Kurnosikov,[3] Alexander Haas,[1] Ryohei Nemoto,[4] Toyo Kazu Yamada,[4,5] Jörg Schmalian,[2,6] and Wulf Wulfhekel[1,2]

[1]*PHI, Karlsruhe Institute of Technology, 76131 Karlsruhe, Germany*
[2]*IQMT, Karlsruhe Institute of Technology, 76344 Eggenstein-Leopoldshafen, Germany*
[3]*Universite de Lorraine, Institute Jean Lamour, 54011 Nancy Cedex, France*
[4]*Department of Materials Science, Chiba University, Chiba 263-8522, Japan*
[5]*Molecular Chirality Research Centre, Chiba University, Chiba 263-8522, Japan*
[6]*TKM, Karlsruhe Institute of Technology, 76131 Karlsruhe, Germany*

(Received 7 July 2025; accepted 8 December 2025; published 4 February 2026)

The majority of superconductors have more than one Fermi surface, on which the electrons pair below the critical temperature, yet their behavior can be well described by a single-band Bardeen-Cooper-Schrieffer theory. This is mostly due to interband scattering, especially in superconductors in the dirty limit, rigidly linking the pairing amplitude of the bands. This has limited experimental studies of the complex physics of multiband superconductivity. Here, we utilize the fact that elementary Pb—as a clean limit system—has two Fermi surfaces that are only weakly coupled by interband scattering, allowing the formation of two separate condensates. By studying stacking fault tetrahedra with a millikelvin scanning tunneling microscope, we show how to locally tune interband coupling ranging from weak to strong coupling and modify the superconducting order parameters from two well separated gaps to one merged gap around defects. The experiments critically test the theory of multiband superconductors and give a route to access a wide range of predicted quantum effects in these systems.

DOI: 10.1103/4vhj-s1fq

Microscopic attractive interactions between electrons that lead to conventional superconductivity are captured by the Bardeen-Cooper-Schrieffer (BCS) theory [1], which successfully predicts the temperature dependence of the superconducting gap or the shape of the quasiparticle spectrum. In some sense, the theory performs even better than expected. Although, in its most elementary form, it considers a single electronic band and a perfectly clean environment, it still describes the tunneling spectra measured on many real superconductors. As an extension, the finite effective quasiparticle lifetimes, e.g., due to scattering by nonmagnetic imperfections or inelastic scattering processes, were also considered by Dynes and others [2,3]. Most superconductors have more than one Fermi surface leading to superconductivity in multiple bands. Multiband superconductivity was first suggested by Suhl, Matthias, and Walker (SMW) [4], only two years after the seminal theory by BCS, and highlighted the case of two noninteracting bands. Without interband pairing interaction, the individual bands are expected to develop distinct superconducting gaps that emerge at distinct transition temperatures (T_c) [4]. The reason behind the single-band BCS theory's long success lies in the fact that scattering between multiple bands couples these distinct pairing amplitudes which emerge at a single T_c. In the limit of strong coupling, the gap values merge to a common value due to an interband proximity effect in momentum space [5–8]. This process can be due to interband electron-phonon or electron-electron interactions in clean systems. It becomes unavoidable in "dirty" superconductors or at temperatures close to T_c, where electron lifetimes become shorter, leading to the appearance of a single pairing condensate with essentially a single lifetime-broadened superconducting gap [4,5,9,10] that disguises the multiband nature of the material. According to Anderson's theorem, the gap and the transition temperature are robust against nonmagnetic scatterings for single-band conventional superconductors [11]. However, in full agreement with our above statements, generalizations to multiband superconductors show that nonmagnetic scattering changes the superconducting gap values as long as their magnitudes are distinct [12]. Robustness against nonmagnetic impurities reemerges once a common gap value has been established.

With advances in the growth of high-quality superconductor crystals and improvements in low-temperature measurement techniques, it has become possible to discern

*These authors contributed equally to this work.
†Contact author: qili.li@kit.edu

the energy differences among individual superconducting gaps in several multiband systems [13–17], such as MgB_2 and iron-based superconductors. While there is a consensus that interband scattering is crucial for the pairing in iron-based superconductors [18], a systematic study that critically tests the multigap superconductivity theory against local tunneling spectra has so far been prevented by its anisotropic gap function [19,20], unconventional pairing mechanism [19–21], and obstructing quasiparticle states [22]. In MgB_2, the geometry and orbital character of the disjoint π and σ Fermi surface sheets naturally suppress interband scattering [23] and a high defect density as well as randomly oriented grains in real samples complicate a systematic experimental study. Among the viable materials, bulk lead (Pb) stands out as an elemental two-band superconductor that is available in exceptional purity and crystallinity [17,24–26]. Pb displays two Fermi surfaces, an open one (OFS) and a compact one (CFS) [Figs. 1(c) and 1(d)] [27]. Recent experiments further indicate that the interband coupling in Pb is rather weak [26], such that at low temperatures, two superconducting gaps appear. The CFS of Pb gives rise to the larger gap (Δ_2) and the OFS to the smaller one (Δ_1) [25,26]. This makes Pb an ideal model system for experimentally studying how two bands and their condensates interact, e.g., by studying how individual crystal defects alter the scattering within and between bands and change the pairing state. This direct insight into the microscopic scattering events is not only of importance for conventional but also for unconventional superconductors because in multiband systems with sign-reversing order parameter, like the iron-based superconductors, even nonmagnetic interband scatterers cause pair breaking [18].

Clean and flat Pb(111) surfaces were prepared in vacuum and measured at 43 mK with a home-built scanning tunneling microscopy (STM) [26,28] (see Supplemental Material (SM) Note I [29]). In STM topography [cf. Fig. 1(a)], we can see three types of defects: (i) small depressions of hexagonal shape due to argon bubbles or vacancy conglomerates near the surface [30,31]; (ii) a screw dislocation, of which both ends exit the surface [32–34]; (iii) a buried stacking fault tetrahedron (SFT1) of about 70 nm lateral width [32,35–37], which essentially is an embedded fcc twin with stacking faults on its four triangular surfaces [38–49], binding the screw dislocation [32,45] and causing the weak interference pattern visible in Fig. 1(a) (see SM Notes I and II [29]). A characteristic of SFT near the surface is the quantum well states (QWS) [50,51] that form between its triangular top (111) plane and the (111) sample surface (see SM Note III [29]). It is well established that these QWS allow to image subsurface defects, including SFT, with STM and to determine their depths below the surface [30,36,37,52–55]. A sketch of the measurement principle is shown in Fig. 1(b).

Beyond the modulation of the local DOS (LDOS) due to the QWS on an energy scale of hundreds of meV, an SFT also locally influences superconductivity. Differential conductance (dI/dU) maps at bias voltages of the bulk coherence peaks at Δ_1^0 ($U = 1.25$ mV) and Δ_2^0 ($U = 1.40$ mV) [17,26,56] reveal SFTs through remarkable features in the LDOS on energy scales related to the superconducting gaps (see SM [29] Note IV). As can be seen in Figs. 1(c) and 1(d), they feature a hexagonal region of decreased LDOS at Δ_1^0 (c) and increased LDOS at Δ_2^0

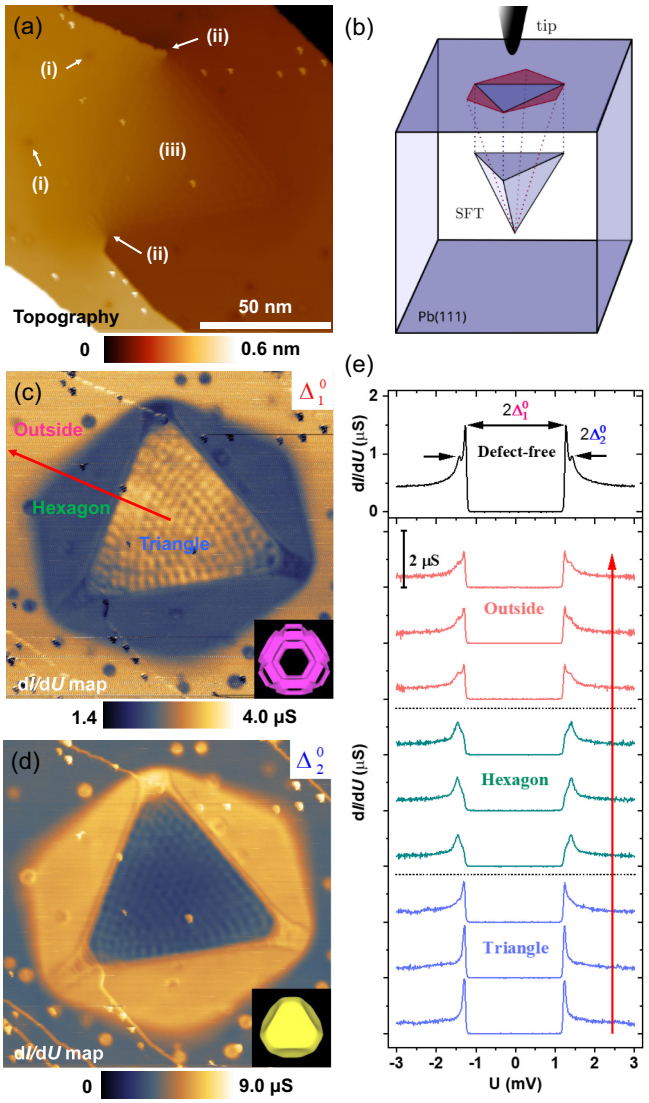

FIG. 1. Influence of an SFT on superconducting gaps (SFT1). (a) Topography ($U = 1.4$ mV, $I = 1$ nA). Defects are indicated as (i) argon bubbles or small vacancy conglomerates, (ii) a screw dislocation, and (iii) a buried SFT. (b) Sketch of the STM measuring a subsurface SFT in Pb(111). (c) dI/dU map at Δ_1^0. (d) dI/dU map at Δ_2^0. (c),(d) Insets show the corresponding open/compact Fermi surfaces [27]. dI/dU maps are tip stabilized at $U = 1.4$ mV, $I = 1$ nA modulation $U_{\mathrm{mod}} = 50$ μV at 3.751 kHz). (e) dI/dU spectra on defect-free area (top panel) and at different regions from triangle center to outside the SFT along the red arrow in panel (c) ($U = 3$ mV, $I = 1$ nA, $U_{\mathrm{mod}} = 20$ μV).

(d). We point out that screw dislocations have no influence on the superconducting states in Pb(111) (see SM Note V [29]). The SFT top plane appears as a triangular cutout within the hexagon with slightly higher/lower LDOS in Figs. 1(c) and 1(d) and a visible quasiparticle interference (QPI) pattern. The rodlike contours of the LDOS can be seen along the sides of the inner triangle and along the $[10\bar{1}]$, $[01\bar{1}]$ and $[\bar{1}10]$ directions inside the outer hexagon and may be related to the stair-rod dislocations of the SFT (see SM Note II [29]). These features in $\mathrm{d}I/\mathrm{d}U$ maps for energies at the corresponding coherence peaks of Pb [17,24–26,56] indicate a local change in the spectral gap Δ or in the intensity of the coherence peak. The top panel of Fig. 1(e) shows such a spectrum recorded far away from any defects [17,26]. Taking spectra along the red line indicated in Fig. 1(c) confirms that the contrast in the $\mathrm{d}I/\mathrm{d}U$ maps in Figs. 1(c) and 1(d) stems from changes in the quasiparticle spectrum of the superconductor, i.e. the intensity and energy of the coherence peaks [Fig. 1(e)]. In the triangle region, the coherence peak of the smaller gap is very pronounced, while the coherence peak of the larger gap is suppressed. In the hexagonal region, the behavior is the opposite. In the outside region, the spectra gradually tend to the defect-free tunneling spectra on Pb(111).

In a two-band superconductor, the observed behavior can be either due to changes in the STM tunneling matrix element or a local change in the pairing condensate. Here, the former is not at play as the probed surface is of (111) orientation on and next to the SFT. Moreover, also the energies of the coherence peaks vary, speaking clearly for a modification of the condensates. For more details see SM Notes VIII–X [29].

To understand our experimental tunneling spectra of the two-band superconductor Pb(111), we performed simulations of the density of states of an impurity-coupled two-band superconductor, following the work of Sung and Wong (S&W model) [5,7,13,16,57–64]. It describes an interband proximity effect in a two-band superconductor induced by elastic interband scattering events with rates Γ_{ij} at nonmagnetic impurities but also includes intraband scattering rates Γ_i (see SM Notes I, VI, and VII [29]). The model features coupled equations of the two order parameters. This leads to an interband proximity effect in the k space that couples the two condensates. As a consequence, the individual gap functions Δ_1 and Δ_2 become complex and energy dependent.

To illustrate the interband proximity effect, we show model calculations in Figs. 2(a)–2(c) with varying interband scattering, where the intrinsic gaps ($\Delta_1^0 = 1.252$ meV and $\Delta_2^0 = 1.40$ meV) and effective temperature ($T = 139$ mK) were obtained from defect-free areas by fitting using the S&W model (see SM Notes I and IV [29]). The three panels display the normalized single particle DOS with different interband couplings and for two different values of the ratio $\eta = N_2(E_F)/N_1(E_F)$.Naturally, for larger η the higher

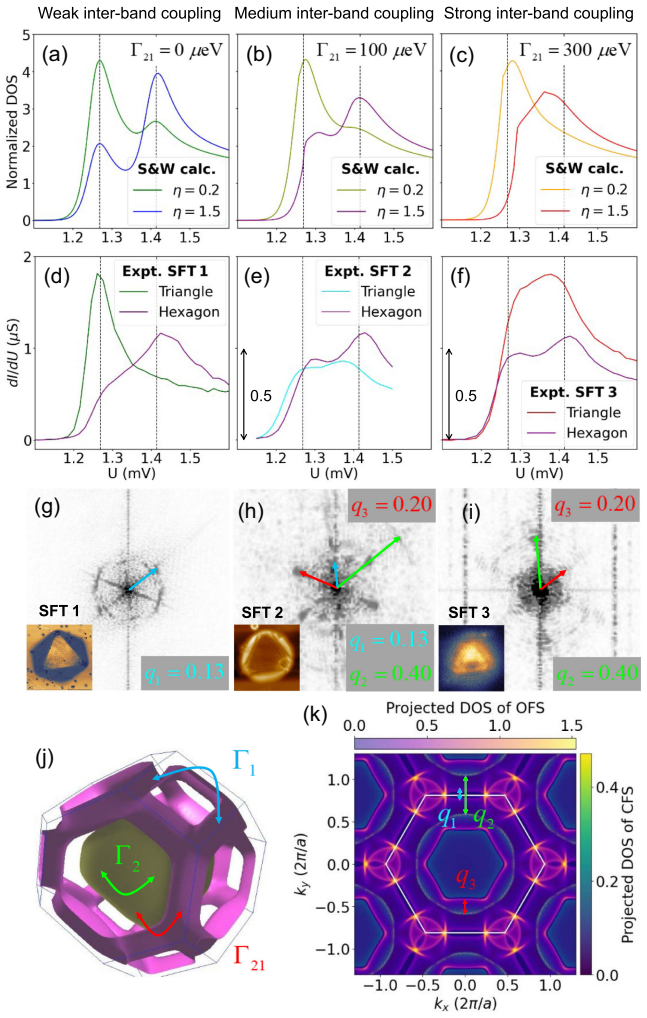

FIG. 2. Influence of scattering on two-band superconducting gaps. (a)–(c) Model results for two coupled superconducting gaps with different DOS ratio η from weak (a) to strong (c) interband coupling Γ_{21}. The green to orange color corresponds to increasing interband coupling for low η. The blue to red color corresponds to increasing interband coupling for high η. (d)–(f) Spectra at triangle and hexagon regions for three different SFTs. (d) Tunneling parameters as in Fig. 1, (e),(f) $U = 100$ mV, $I = 1$ nA, $U_{\mathrm{mod}} = 20$ μV with an extra tip height (z) offset of −120 pm. (g)–(i) QPI patterns with unit $2\pi/a$ for $\boldsymbol{q}_1$, $\boldsymbol{q}_2$ and $\boldsymbol{q}_3$.Insets are the corresponding $\mathrm{d}I/\mathrm{d}U$ maps measured at Δ_1^0 (SFT1), Δ_2^0 (SFT2) and Δ_2^0 (SFT3), respectively. (j) Sketch of defect-induced inter- and intraband scattering on the CFS and OFS with Fermi surfaces from Ref. [27]. (k) Calculated projected DOS of OFS and CFS. k_x, k_y, and k_z are in $[1\bar{1}0]$, $[11\bar{2}]$, and $[111]$ direction, respectively. The green/cyan arrows are the nesting vectors of intraband scattering for CFS/OFS. The red arrow is the nesting vector of interband scattering.

energy coherence peak is more pronounced. For $\Gamma_{21} = 0$, the two gaps are fully decoupled, and the total spectrum is just the sum of two BCS gap functions [Fig. 2(a)]. With increasing Γ_{21}, the two gaps begin to merge [Fig. 2(b)] and eventually become indistinguishable [Fig. 2(c)].

With the above illustration, we are able to explain our experimental tunneling spectra for different SFTs. The spectra of three representative SFTs are shown in Figs. 2(d)–2(f). In the hexagonal region, cf. purple curves in Figs. 2(d)–2(f), an intermediate coupling brings the two gaps closer. In addition, a large η makes the coherence peak intensity of Δ_2 higher than that of Δ_1. However, in the triangular region, the interband coupling and η vary from weak [green curve in Fig. 2(d)] to strong [red curve in Fig. 2(f)]. This is due to the QWS confined above the SFT that leads to a pronounced scattering and a modulation in the DOS of the CFS, which can vary from a minimum to maximum depending on the depth of SFT (see SM Note III [29]). For the weak interband coupling and very low η, only an unshifted Δ_1 is observed [green curve in Fig. 2(d)]. For medium interband coupling and medium η, two gaps move towards each with comparable coherence peak intensity [magenta curve in Fig. 2(e)]. Eventually, for the strong interband coupling, the gaps have merged completely, shown as red curve in Fig. 2(f). We point out that intraband scattering only plays a role in broadening the coherence peaks (see SM Note VII [29]).

QPI patterns can be seen in the triangle in Figs. 1(c) and 1(d). We point out that these are not due to superconducting states and are not pair density waves, as they do not change when superconductivity is suppressed by a magnetic field (see SM Notes VIII and IX [29]). Therefore, these patterns arise from the scattering of unpaired quasiparticles around the Fermi energy. To quantify the QPI, we Fourier transformed the $\mathrm{d}I/\mathrm{d}U$ maps and compare them with the nesting vectors of the projected DOS of the surface Brillouin zone [65–70]. Figures 2(g)–2(i) show the QPI patterns in reciprocal space.

In SFT1, as discussed in [Figs. 2(a) and 2(d)], η is low in the triangle. This indicates that there the DOS on the CFS is small compared to the OFS. Therefore, only intraband scattering on the OFS is observed. The wave vector (cyan arrow) in Fig. 2(g) matches very well in Fig. 2(k).

In contrast, for SFT2 [Figs. 2(b) and 2(e)], the DOS ratio on the CFS and OFS is comparable, so both interband scattering between the CFS and OFS and intraband scattering on each Fermi surface are possible and are observed in Fig. 2(h). All three wave vectors can be related to the nesting vectors in Fig. 2(k), $\boldsymbol{q}_1$ (cyan arrow) and $\boldsymbol{q}_2$ (green arrow) correspond to intraband scattering on the OFS [see also cyan arrow in Fig. 2(j)] and CFS [see also green arrow in Fig. 2(j)], respectively. $\boldsymbol{q}_3$ is the interband scattering vector (red arrow) in Fig. 2(k). These results are consistent with our previous analysis of the superconducting spectra; i.e., that medium intra- and interband scattering is present in the triangle region.

Lastly, we come to SFT3 with strong interband coupling in the triangle. Here, η is large [Figs. 2(c) and 2(f)] compared to the previous two cases. This indicates that the DOS on the CFS is large compared to the OFS. For these reasons, we can expect to observe both inter- and intraband scattering. However, the intraband scattering on the OFS might not be visible due to is lower DOS. And indeed, here we only find $\boldsymbol{q}_1$ and $\boldsymbol{q}_2$ but not $\boldsymbol{q}_3$ [Fig. 2(i)].

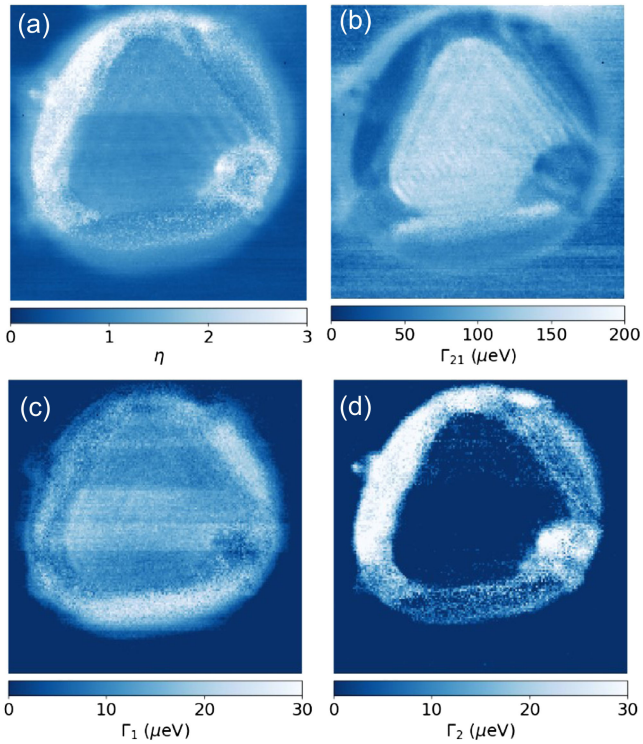

FIG. 3. High-resolution images of local scattering rates for SFT2. (a) Spatially resolved DOS ratio η, (b) interband coupling Γ_{21} (see Fig. 2(j)), (c) intraband coupling Γ_1 for OFS [see Fig. 2(j)], and (d) intraband coupling Γ_2 for CFS [see Fig. 2(j)].

On SFT2 shown in Fig. 2, we recorded dI/dU spectra in a finely spaced grid and fitted them to the S&W model DOS to obtain locally resolved information on the inter- and intraband scattering rates for each point and visualize them in a 2D map around the SFT. The results are presented in Fig. 3 (see SM Note VIII [29]). The defect induces local variations of the DOS ratio η, as well as inter- and intraband scattering. Notably, η is significantly enhanced in the hexagonal region [Fig. 3(a)] and interband scattering is enhanced in both the hexagon and triangle region [Fig. 3(b)]. The induced interband scattering leads to a measurable interband proximity effect. The numerical values of Γ_{21} place these regions in the medium interband coupling regime. Intraband scattering is responsible for broadening the coherence peaks (see SM Note VII [29]). Intraband scattering on the OFS (Γ_1) is enhanced in the hexagonal and the triangular region [Fig. 3(c)], while on the CFS (Γ_2), it is only enhanced in the hexagonal region [Fig. 3(d)]. We did an analogous measurement on the small SFT3 with strong interband coupling and show the resulting maps in SM Note IX [29].

Our results show that a stacking fault locally alters the superconducting properties in a multiband system via drastic changes in the intra- and interband coupling in agreement with the S&W model [5] [see Fig. 2(k)]. The intraband coupling is mostly responsible for lifetime broadening of the individual coherence peaks (see SM Note VII [29]), while the interband coupling changes their relative energies (see Fig. 2). Eventually, strong interband coupling merges the gap magnitudes to a common value, making the density of states indistinguishable from the one of a single band system [see Figs. 2(c) and 2(f)]. Intra- and interband scattering events can be understood on basis of the two Fermi surfaces [see Fig. 2(j)]. At a stacking fault, electrons of each band will be partially reflected staying on the same band, but can also be scattered to the other band. Fits to the S&W model show an enhancement of the interband scattering Γ_{21} on top of the whole stacking fault of the SFT, i.e., the triangular region in Fig. 3(b), corresponding to the medium interband coupling shown in Fig. 2. This enhanced interband scattering extends even beyond the SFT, most likely due to electronic states with a finite momentum parallel to the surface. Note that Γ_{ij} need to conserve the total number of electrons on each band; i.e., they are proportional to the DOS of each band. Intraband scattering, however, may independently vary on each band as the reflection probability of Bloch states on the two bands by a stacking fault depends on the dispersion of the respective band. This is also reflected by the difference in the pattern of Figs. 3(c) and 3(d). Due to the more symmetric shape of the CFS [see Fig. 2(j)], reflection at stacking faults is less expressed in comparison to the more asymmetric structure of the OFS [see Fig. 2(j)]. This is reflected in the generally higher values for intraband scattering Γ_1 in the triangle region. Similarly, intraband scattering is visible in the hexagonal region showing standing waves corresponding to the CFS.

Our study demonstrates that SFTs, i.e., twin crystals, in Pb allow for the exploration of interband scattering strengths, crucial for understanding the interband proximity effect parameter Γ_{ij}. The experimental results confirm the model by Sung and Wong, providing the first direct observation of the interband proximity effect at the nanoscale. QPI patterns including corresponding intra- and interband scattering vectors reinforce our conclusions. Both extremes, i.e., mostly decoupled condensates with two independent gaps and fully coupled condensates with only a single gap, can be realized in near proximity to each other in the same material. In light of the recent popularity in pair density wave states [71], we also conclude that scattering at a stacking fault causes a real space modulation of the density of states ratio of the two bands, ultimately leading to a weak modulation of the coherence peak position. This is a natural consequence in the interband proximity effect but we show that it has its roots in normal state scattering. We expect that crystal defects in other two band superconductors can have a similar effect on the LDOS. Such a defect can in principle also act in the opposite way; i.e., a superconductor with strong intrinsic interband scattering may see it weakened at the defect. We demonstrated the tunability of the interband coupling ranging from weak (SFT1) to strong (SFT3). Gaining control over the interband coupling and scattering processes may even give access to a wide range of predicted quantum effects, such as solitons [72,73], vortices with fractional flux [74], non-Abrikosov vortices [75], topological knots [75], or the Leggett mode that describes excitations of the relative phase of weakly coupled bands [76].

Acknowledgments—We are grateful for discussions with Roland Willa, Horst Hahn, Marcel Rost, and Reinhard Schneider. The authors acknowledge funding by the Deutsche Forschungsgemeinschaft (DFG) under the CRC TRR 288–422213477 grant "ElastoQMat," projects B06 and B01, and support by JSPS KAKENHI under Grant No. 17K19023.

Data availability—The data are available from the authors upon reasonable request.

[1] J. Bardeen, L. N. Cooper, and J. R. Schrieffer, Phys. Rev. **106**, 162 (1957).
[2] R. C. Dynes, V. Narayanamurti, and J. P. Garno, Phys. Rev. Lett. **41**, 1509 (1978).
[3] F. Herman and R. Hlubina, Phys. Rev. B **94**, 144508 (2016).
[4] H. Suhl, B. T. Matthias, and L. R. Walker, Phys. Rev. Lett. **3**, 552 (1959).
[5] C. C. Sung and V. K. Wong, J. Phys. Chem. Solids **28**, 1933 (1967).
[6] W. L. McMillan, Phys. Rev. **175**, 537 (1968).
[7] N. Schopohl and K. Scharnberg, Solid State Commun. **22**, 371 (1977).
[8] C. Noce and L. Maritato, Phys. Rev. B **40**, 734 (1989).
[9] I. M. Tang, Phys. Rev. B **2**, 129 (1970).
[10] W. S. Chow, Phys. Rev. B **4**, 111 (1971).
[11] P. W. Anderson, J. Phys. Chem. Solids **11**, 26 (1959).
[12] M. Hoyer, M. S. Scheurer, S. V. Syzranov, and J. Schmalian, Phys. Rev. B **91**, 054501 (2015).
[13] M. Iavarone, G. Karapetrov, A. E. Koshelev, W. K. Kwok, G. W. Crabtree, D. G. Hinks, W. N. Kang, E.-M. Choi, H. J. Kim, H.-J. Kim, and S. I. Lee, Phys. Rev. Lett. **89**, 187002 (2002).
[14] T. Hanaguri, K. Kitagawa, K. Matsubayashi, Y. Mazaki, Y. Uwatoko, and H. Takagi, Phys. Rev. B **85**, 214505 (2012).
[15] Q.-Y. Wang, Z. Li, W.-H. Zhang, Z.-C. Zhang, J.-S. Zhang, W. Li, H. Ding, Y.-B. Ou, P. Deng, K. Chang, J. Wen, C.-L. Song, K. He, J.-F. Jia, S.-H. Ji, Y.-Y. Wang, L.-L. Wang, X. Chen, X.-C. Ma, and Q.-K. Xue, Chin. Phys. Lett. **29**, 037402 (2012).
[16] Y. Noat, J. A. Silva-Guillén, T. Cren, V. Cherkez, C. Brun, S. Pons, F. Debontridder, D. Roditchev, W. Sacks, L. Cario, P. Ordejón, A. García, and E. Canadell, Phys. Rev. B **92**, 134510 (2015).

[17] M. Ruby, B. W. Heinrich, J. I. Pascual, and K. J. Franke, Phys. Rev. Lett. **114**, 157001 (2015).
[18] P. J. Hirschfeld, M. M. Korshunov, and I. I. Mazin, Rep. Prog. Phys. **74**, 124508 (2011).
[19] I. I. Mazin, D. J. Singh, M. D. Johannes, and M. H. Du, Phys. Rev. Lett. **101**, 057003 (2008).
[20] A. D. Christianson, E. A. Goremychkin, R. Osborn, S. Rosenkranz, M. D. Lumsden, C. D. Malliakas, I. S. Todorov, H. Claus, D. Y. Chung, M. G. Kanatzidis, R. I. Bewley, and T. Guidi, Nature (London) **456**, 930 (2008).
[21] A. V. Chubukov, D. V. Efremov, and I. Eremin, Phys. Rev. B **78**, 134512 (2008).
[22] J. Lee, S. Lee, A. Kreisel, J. Paaske, B. M. Andersen, K. M. Bastiaans, D. Chatzopoulos, G. Gu, D. Cho, and M. P. Allan, Nano Lett. **25**, 4227 (2025).
[23] I. I. Mazin, O. K. Andersen, O. Jepsen, O. V. Dolgov, J. Kortus, A. A. Golubov, A. B. Kuz'menko, and D. van der Marel, Phys. Rev. Lett. **89**, 107002 (2002).
[24] A. Floris, A. Sanna, S. Massidda, and E. K. U. Gross, Phys. Rev. B **75**, 054508 (2007).
[25] T. G. Saunderson, J. F. Annett, B. Újfalussy, G. Csire, and M. Gradhand, Phys. Rev. B **101**, 064510 (2020).
[26] T. Gozlinski, Q. Li, R. Heid, R. Nemoto, R. Willa, T. K. Yamada, J. Schmalian, and W. Wulfhekel, Sci. Adv. **9**, eadh9163 (2023).
[27] T.-S. Choy, J. Naset, J. Chen, S. Hershfield, and C. Stanton, Bull. Am. Phys. Soc. **45**, L36 (2000), http://www.phys.ufl.edu/fermisurface/.
[28] T. Balashov, M. Meyer, and W. Wulfhekel, Rev. Sci. Instrum. **89**, 113707 (2018).
[29] See Supplemental Material at http://link.aps.org/supplemental/10.1103/4vhj-s1fq for Notes I-X.
[30] M. Müller, N. Néel, S. Crampin, and J. Kröger, Phys. Rev. Lett. **117**, 136803 (2016).
[31] S. Y. Song and J. Seo, Sci. Rep. **7**, 12177 (2017).
[32] J. F. Wolf and H. Ibach, Appl. Phys. A **52**, 218 (1991).
[33] J. Engbæk, J. Schiøtz, B. Dahl-Madsen, and S. Horch, Phys. Rev. B **74**, 195434 (2006).
[34] A. Y. Aladyshkin, A. S. Aladyshkina, and S. I. Bozhko, J. Phys. Chem. C **125**, 26814 (2021).
[35] M. Ohmori, H. Hirayama, and K. Takayanagi, Phys. Rev. B **59**, 5612 (1999).
[36] K. Schouteden and C. Van Haesendonck, Phys. Rev. Lett. **108**, 076806 (2012).
[37] K. Schouteden, B. Amin-Ahmadi, Z. Li, D. Muzychenko, D. Schryvers, and C. Van Haesendonck, Nat. Commun. **7**, 14001 (2016).
[38] J. Silcox and P. B. Hirsch, Philos. Mag. **4**, 72 (1959).
[39] R. M. J. Cotterill, Philos. Mag. **6**, 1351 (1961).
[40] M. J. Yokota and J. Washburn, Philos. Mag. **16**, 459 (1967).
[41] F. Bonsignori, V. Bortolani, and G. Velo, Nuovo Cimento B **57**, 194 (1968).
[42] Q. F. Guan, L. Pan, H. Zou, A. M. Wu, S. Z. Hao, Q. Y. Zhang, C. Dong, and G. T. Zou, J. Mater. Sci. **39**, 6349 (2004).
[43] R. Schäublin, Z. Yao, N. Baluc, and M. Victoria, Philos. Mag. **85**, 769 (2005).
[44] G. J. Hardy and M. L. Jenkins, Philos. Mag. **52**, L19 (2006).
[45] Y. N. Osetsky, D. Rodney, and D. J. Bacon, Philos. Mag. **86**, 2295 (2006).
[46] B. P. Uberuaga, R. G. Hoagland, A. F. Voter, and S. M. Valone, Phys. Rev. Lett. **99**, 135501 (2007).
[47] Y. Matsukawa, Y. N. Osetsky, R. E. Stoller, and S. J. Zinkle, Philos. Mag. **88**, 581 (2008).
[48] J. Wei Wang, S. Narayanan, J. Yu Huang, Z. Zhang, T. Zhu, and S. X. Mao, Nat. Commun. **4**, 2340 (2013).
[49] K. Y. Yu, D. Bufford, C. Sun, Y. Liu, H. Wang, M. A. Kirk, M. Li, and X. Zhang, Nat. Commun. **4**, 1377 (2013).
[50] Y. Guo, Y.-F. Zhang, X.-Y. Bao, T.-Z. Han, Z. Tang, L.-X. Zhang, W.-G. Zhu, E. G. Wang, Q. Niu, Z. Q. Qiu, J.-F. Jia, Z.-X. Zhao, and Q.-K. Xue, Science **306**, 1915 (2004).
[51] M. Schackert, T. Märkl, J. Jandke, M. Hölzer, S. Ostanin, Eberhard K. U. Gross, A. Ernst, and W. Wulfhekel, Phys. Rev. Lett. **114**, 047002 (2015).
[52] O. Kurnosikov, O. A. O. Adam, H. J. M. Swagten, W. J. M. de Jonge, and B. Koopmans, Phys. Rev. B **77**, 125429 (2008).
[53] O. Kurnosikov, J. H. Nietsch, M. Sicot, H. J. M. Swagten, and B. Koopmans, Phys. Rev. Lett. **102**, 066101 (2009).
[54] O. Kurnosikov, H. J. M. Swagten, and B. Koopmans, Phys. Rev. Lett. **106**, 196803 (2011).
[55] A. Weismann, M. Wenderoth, S. Lounis, P. Zahn, N. Quaas, R. G. Ulbrich, P. H. Dederichs, and S. Blügel, Science **323**, 1190 (2009).
[56] M. Uhl, P. Kot, R. Drost, H. Huang, J. Ankerhold, J. C. Cuevas, and C. R. Ast, Phys. Rev. Res. **6**, 043233 (2024).
[57] H. Schmidt, J. F. Zasadzinski, K. E. Gray, and D. G. Hinks, Phys. Rev. Lett. **88**, 127002 (2002).
[58] T. Ekino, T. Takasaki, T. Muranaka, J. Akimitsu, and H. Fujii, Phys. Rev. B **67**, 094504 (2003).
[59] H. Schmidt, J. F. Zasadzinski, K. E. Gray, and D. G. Hinks, Physica (Amsterdam) **385C**, 221 (2003).
[60] J. A. Silva-Guillén, Y. Noat, T. Cren, W. Sacks, E. Canadell, and P. Ordejón, Phys. Rev. B **92**, 064514 (2015).
[61] Y. Noat, T. Cren, F. Debontridder, D. Roditchev, W. Sacks, P. Toulemonde, and A. San Miguel, Phys. Rev. B **82**, 014531 (2010).
[62] J. Senkpiel, C. Rubio-Verdú, M. Etzkorn, R. Drost, L. M. Schoop, S. Dambach, C. Padurariu, B. Kubala, J. Ankerhold, C. R. Ast, and K. Kern, Phys. Rev. B **100**, 014502 (2019).
[63] Y. Noat, T. Cren, P. Toulemonde, A. San Miguel, F. Debontridder, V. Dubost, and D. Roditchev, Phys. Rev. B **81**, 104522 (2010).
[64] S. Datta, A. Vasdev, S. Halder, J. Singh, Y. Singh, and G. Sheet, J. Phys. Condens. Matter **32**, 315701 (2020).
[65] L. Kleinman, Phys. Rev. B **21**, 2630 (1980).
[66] D. Vanderbilt, Phys. Rev. B **32**, 8412 (1985).
[67] C. Elsasser, N. Takeuchi, K. M. Ho, C. T. Chan, P. Braun, and M. Fahnle, J. Phys. Condens. Matter **2**, 4371 (1990).
[68] J. P. Perdew and Y. Wang, Phys. Rev. B **45**, 13244 (1992).
[69] B. Meyer and M. Fähnle, Phys. Rev. B **56**, 13595 (1997).
[70] R. Heid, K. P. Bohnen, I. Y. Sklyadneva, and E. V. Chulkov, Phys. Rev. B **81**, 174527 (2010).
[71] D. F. Agterberg, J. C. S. Davis, S. D. Edkins, E. Fradkin, D. J. Van Harlingen, S. A. Kivelson, P. A. Lee, L. Radzihovsky, J. M. Tranquada, and Y. Wang, Annu. Rev. Condens. Matter Phys. **11**, 231 (2020).
[72] Y. Tanaka, Phys. Rev. Lett. **88**, 017002 (2001).

[73] S. V. Kuplevakhsky, A. N. Omelyanchouk, and Y. S. Yerin, Low Temp. Phys. **37**, 667 (2011).
[74] E. Babaev, Phys. Rev. Lett. **89**, 067001 (2002).
[75] Y. M. Cho and P. Zhang, Phys. Rev. B **73**, 180506(R) (2006).
[76] A. J. Leggett, Prog. Theor. Phys. **36**, 901 (1966).